Chapter-VI

6.1 Introduction

As discussed in Chapter I, single phase multiferroics exhibit very weak magnetoelectric (ME) response. Most of them show their multiferroic behaviour well below room temperature and are unsuitable for device applications at ambient temperature [Rado and Folen (1961); Rado and Folen (1962); Freeman and Schmid (1975); Smolenskii and Chupis (1984); Siratori et al. (1992); Kumar et al. (1998); Suryanarayana (1994)]. This drawback of single phase multiferroics forces the researchers to investigate some new materials which exhibit high ME response at ambient temperature. In recent years, multiferroic composites have been attracted considerable interest due to the coupled ferroelectric and magnetic response leading to magnetoelectric (ME) behaviour [Boomgard and Born (1978); Kumar et al. (1998)]. Magnetoelectric coupling in multiferroic composites is a multiplicative property of the ferroelectric and magnetic phases mechanically mediated by strain and neither of the phases exhibit this property individually [Suchtelen (1992); Suryanarayana et al. (1992)]. On application of a magnetic field, magnetostrictive phase changes the shape. The developed strain in this phase is transferred to the piezoelectric phase due to the mechanical contact, which result in polarization in the piezoelectric phase [Nan et al. (2008); Wang et al. (2010)]. Similarly, on the application of electric field, the piezoelectric material develops strain which is transferred to the magnetostrictive phase, resulting in magnetization. Following this principle, several multiferroic composites have been synthesized taking the suitable combination of

ferroelectric and magnetostrictive systems such as $BaTiO_3/CoFeO_4$ [Boomgaard et al. (1976); Nan (1994); Suryanarayana et al. (1994)], $PbZr_xTi_{1-x}O_3/Ni_{1-y}Zn_yFe_2O_4$ [Srinivasan et al. (2001); Chougule and Chougule (2008); Pandey et al. (2014)], $(1-x)Pb(Mg_{1/3}Nb_{2/3})O_3-xPbTiO_3/ Ni_{1-y}Zn_yFe_2O_4$ [Paik (1997); Sheikh and Mathe (2009)], $PbTiO_3/ Ni_{1-y}Zn_yFe_2O_4$ [Zhang et al. (2010)] etc.

In this Chapter, we have discussed the synthesis of different compositions of the multiferroic particulate composites of $0.51Bi(Ni_{1/2}Ti_{1/2})O_3-0.49PbTiO_3$ (BNT-PT) with $Ni_{0.6}Zn_{0.4}Fe_2O_4$ (NZFO) as $(1-y)0.51Bi(Ni_{1/2}Ti_{1/2})O_3-0.49PbTiO_3/yNi_{0.6}Zn_{0.4}Fe_2O_4$ (BNT-PT/NZFO) and investigated the ferroelectric, magnetic and magnetoelectric (ME) properties. Appearance of (P-E) and (M-H) hysteresis reveal the multiferroic character of the composite. Significant ME-coefficient in (1-y)BNT-PT/yNZFO composites makes it ideal multiferroic material for device application. Our structural analysis reveals that the tetragonality of ferroelectric phase (BNT-PT) enhances with increasing the fraction of magnetic phase (NZFO) in the composite. Large tetragonality is producing the significant strain and strong coupling between ferroelectric and magnetic phases.

6.2. Experimental Details

Samples used in the present work were prepared by conventional solid-state sintering route. Before synthesizing $Ni_{0.6}Zn_{0.4}Fe_2O_4$ (NZFO), Ni-content in the salt $NiCO_3.2Ni(OH)_2$ (Qualigence) has been estimated for which exact assay was not known. $NiCO_3.2Ni(OH)_2$ was heated at 500^0C for 1 hour. Decomposition of $NiCO_3.2Ni(OH)_2$ led to formation of NiO, H_2O and CO_2 as byproducts. The

exact content of Ni in $NiCO_3.2Ni(OH)_2$ was determined to be 42.78%. To prepare $Ni_{0.6}Zn_{0.4}Fe_2O_4$, stoichiometric amounts of AR grade NiO, ZnO (Qualigence, 99%) and Fe_2O_3 (Himedia, 99%) were mixed for 4 hours by ball milling. The powder mixture was calcined at 800^0C for 6 hours. Similarly, $0.51Bi(Ni_{1/2}Ti_{1/2})O_3$-$0.49PbTiO_3$ was prepared by conventional solid state ceramic route as described in Chapter II. Different compositions of (1-y)BNT-PT/yNZFO composites containing $Ni_{0.6}Zn_{0.4}Fe_2O_4$ as a magnetic phase and $0.51Bi(Ni_{1/2}Ti_{1/2})O_3$-$0.49PbTiO_3$ as a ferroelectric phase was prepared by conventional double-sintering method. In this process, the calcined powders of BNT-PT and NZFO were first ball-milled in acetone for 6 hours and then dried. 2% polyvinyl alcohol (PVA) solution in water as binder was mixed with the powders. The powder mixture was pressed into the form of pellets of diameter 12mm and thickness ~ (1.5-2.0)mm using a stainless-steel die and uniaxial hydraulic press at an optimized load of 65kN. Before sintering, the green pellets were kept at 500^0C for 10 hours to burn out the binder. The pellets were finally sintered at 1000^0C for 3 hours. Powder x-ray diffraction (XRD) patterns were recorded using an 18kW rotating anode Cu-target based RIGAKU (Japan) powder x-ray diffractometer fitted with a graphite monochromator in the diffracted beam. For dielectric measurements, the flat surfaces of sintered pellets were gently polished with 0.25μm diamond paste for about 2 minutes and then washed with acetone. Isopropyl alcohol was then applied to clean the surface for removing the moisture, if any, on the pellet surfaces. Fired on silver paste was subsequently applied on both the surface of the pellet. It was first dried around

120^{0}C in an oven and then cured by firing at 500^{0}C for about 5 minutes. To study the ferroelectric properties, dielectric measurements were carried out using Novocontrol, Alpha-A high performance frequency analyzer. Polarization-electric field (P-E) hysteresis measurement was carried out by Radiant (USA) P-E loop tracer. The microstructural studies were done by Zeiss, Supra 40 scanning electron microscope (SEM). Before the microstructural study, sintered pellets were sputter coated with Pd/Au alloys. The dynamic ME response was obtained by changing the DC magnetic field and then measuring the output signal in the form of voltage at applied small AC field of 3Oe. To measure the ME coefficient, the sintered pellets were poled both electrically and magnetically. In electric poling, samples were heated at 100^{0}C in the presence of applied external electric field ~20kV/cm and subsequently cooled to room temperature in the presence of applied electric field. After the electric poling, the samples were poled magnetically at room temperature by applying an external DC-magnetic field of 6kOe. The details of ME set-up and measuring procedure is described in the following Sections 6.3 and 6.4 of this Chapter. FULLPROF program [Carvajal (2011)] was used for Rietveld refinement of the structure. Pseudo-Voight function was used to define the peak profiles and sixth-order polynomial was used to fit the background. In the spinel cubic phase of space group $Fd\bar{3}m$ (Space group # 227), Zn^{2+} and Fe_I^{3+} ions were kept on the tetrahedral 16(c) sites at (1/8, 1/8, 1/8), Fe_{II}^{3+} and Ni^{2+} ions on the octahedral sites 8(b) at (1/2, 1/2, 1/2) and O^{2-} ions on the 32(e) sites at (x, x, x). In the tetragonal phase with P4mm (Space group # 99) space group, the Bi^{3+}/Pb^{2+} ions were kept on 1(a) sites at (0, 0, z),

Ti^{4+}/Ni^{2+} and O_I^{2-} occupy 1(b) sites at (1/2, 1/2, z) and O_{II}^{2-} on the 2(c) sites at (1/2, 0, z).

6.3. Description of ME Measurement Set-up

In the ME measurement set-up (Fig.6.1), Helmholtz coils are mounted on the pole pieces of DC electromagnets. DC magnetic bias field (kOe) is produced by an electromagnet. The electromagnets can be operated using PC interface. To measure the DC field, a Hall probe is used to measure the DC field. Additionally, an AC magnetic field with frequencies in the range of 1 to 10kHz is superimposed onto the DC field. The AC field is produced by a Helmholtz coil, which is driven by an AC current generated by a function generator. The amplitude of the AC field is calculated from the driving current that is measured by a multimeter. The sample is placed in the magnetic field with its surface perpendicular or parallel to the field direction, according to the longitudinal and transverse measurement, respectively. The ME signal was measured using a lock-in amplifier.

6.4. Dynamic Measurement of ME-Coefficient in Multiferroics

Magnetoelectric multiferroics are primarily insulating materials in which electric polarization (P) can be produced by application of AC or DC magnetic field and magnetization (M) can be produced by applying AC or DC electric fields. This phenomenon is termed as magnetoelectric (ME) effect [Kumar et al.
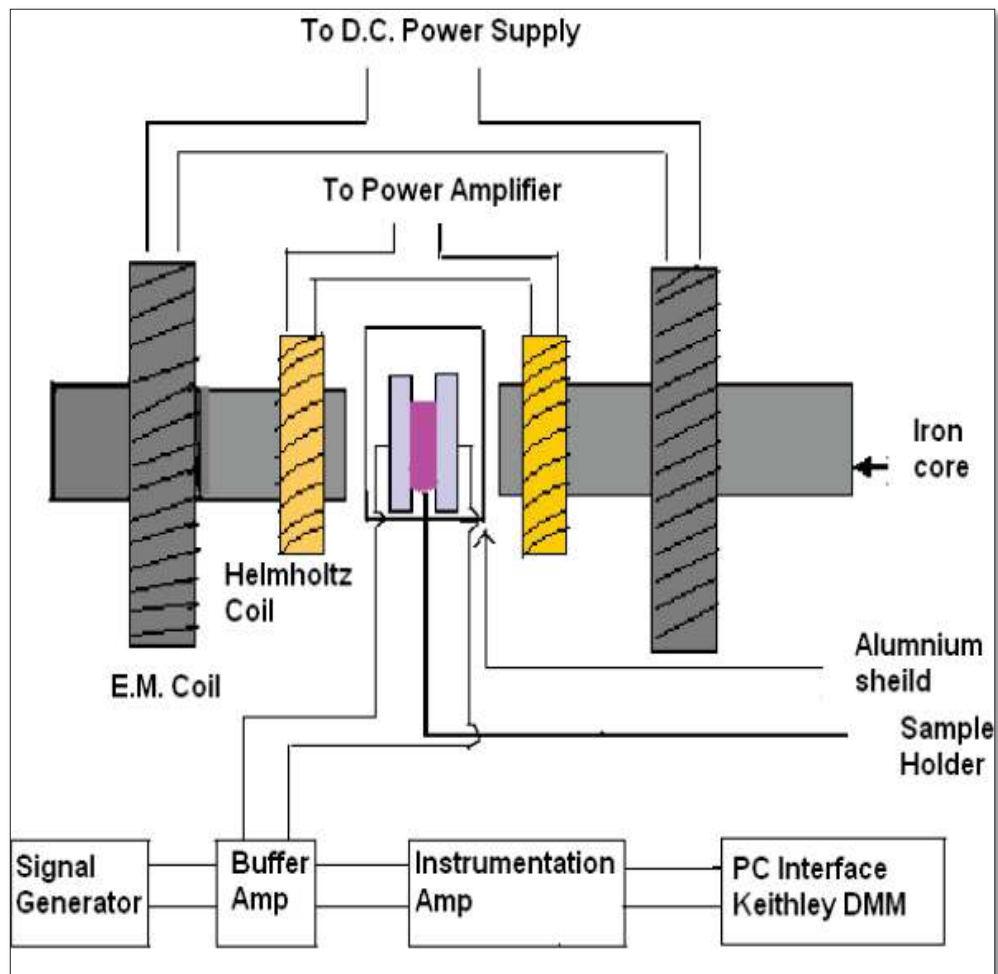
Fig.6.1. Schematic Block diagram of set-up for the dynamic measurement of ME coefficient [after Ramana et al. (2007)].

(1998)]. For ME measurements, it is necessary to pole the sample both eclectically and magnetically by proper poling method. Both linear (α) as well as higher order (β) magnetoelectric coefficients as discussed in Chapter I are possible to measure in multiferroic magnetoelectrics. Three methods (i) Static method [srinivasan et al. (2001); Rado and Folen (1961), (1962); Siratori et al. (1992); Freeman and Schmid (1975)], (ii) Quasi-static method [Rivera (1994); Ye et al. (1994)] and (iii) Dynamic method are adopted to measure the ME response in multiferroic magnetoelectrics [Kumar et al. (1998)]. In the static and quasi-static methods, accumulation of charges at the grain boundary in polycrystalline materials may cause error in the output ME voltage [Hanumaiah et al. (1994); Singh et al. (1994); Suryanarayana (1994); James et al. (1997)].

Schematic block diagram of the ME set-up [Ramana et al. (2007)] for dynamic measurement of ME voltage is shown in Fig.6.1. Dynamic method is an effective method for the measurement of output ME voltage of multiferroic materials. The output ME voltage is measured with time dependent DC magnetic field in the presence of bias AC magnetic field which controls the movement of charges towards the electrode. All other measurements parameters are kept similar to the quasi-static method [Kumar et al. (1998); Rivera (1994)].

Suppose that DC magnetic field H_0 is applied on a polycrystalline ceramic sample. Appeared voltage can be written as [Giap et al. (2007)]

$$V = \text{Const.} + \alpha\, H + \beta\, H^2 + \gamma\, H^3 + \delta\, H^4 + \ldots\ldots\ldots\ldots\ldots\ldots..(6.1)$$

So, $\quad dV/dH = \alpha + 2\,\beta\, H + 3\,\gamma\, H^2 + 4\,\delta\, H^3 + \ldots\ldots\ldots\ldots\ldots\ldots(6.2)$

Where, α and β are linear and quadratic ME coefficients, respectively. γ and δ are higher order ME coefficients. The resultant magnetic field (H_{total}) is the superposition of AC magnetic field ($h_0 \sin(\omega t)$) and DC magnetic field (H_0) which can be written as

$$H_{total} = H + h_0 \sin(\omega t)$$

Now, the appeared voltage in equation (6.1) is given as [Giap et al. (2007)]

$$V = \text{Const.} + \alpha (H + h_0 \sin(\omega t)) + \beta (H + h_0 \sin(\omega t))^2 + \gamma (H + h_0 \sin(\omega t))^3 +$$

$$\delta (H + h_0 \sin(\omega t))^4 + \ldots\ldots\ldots\ldots\ldots\ldots$$

$$= 1/8 \,[(\text{Const.} + 4\,\beta\,h_0^2 + 3\,\delta\,h_0^4 + 8\,\alpha\,H + 12\,\gamma\,h_0^2\,H + 8\,\beta\,H^2 + 24\,\delta\,h_0^2$$

$$H^2 + 8\,\gamma\,H^3 + 8\,\delta\,H^4) + (8\,\alpha\,h_0 + 6\,\gamma\,h_0^3 + 16\,\beta\,h_0\,H + 24\,\delta\,h_0^3\,H + 24\,\gamma$$

$$h_0\,H^2 + 32\,\delta\,h_0\,H^3\,\sin(\omega t)) + \ldots\ldots\ldots\ldots\ldots\ldots\ldots\ldots]$$

The output voltage (V_{out}) obtained by lock-in-amplifier is

$$V_{out} = 1/8 \,(8\,\alpha\,h_0 + 6\,\gamma\,h_0^3 + 16\,\beta\,h_0\,H + 24\,\delta\,h_0^3\,H + 24\,\gamma\,h_0\,H^2 + 32\,\delta\,h_0\,H^3)$$

$$V_{out} = H^4/8 \,[(8\,\alpha\,/\,H^3)\,(h_0\,/\,H) + (6\,\gamma\,/\,H)\,(h_0\,/\,H)^3 + (16\,\beta\,/\,H^2)\,(h_0\,/\,H)$$

$$+\, 24\,\delta\,(h_0\,/\,H)^3 + (24\,\gamma\,/\,H)\,(h_0\,/\,H) + 32\,\delta\,(h_0\,/\,H)]$$

Since ($h_0\,/\,H$) << 1, higher order terms of ($h_0\,/\,H$) can be neglected. Therefore,

$$V_{out} = H^4/8 \,[(8\,\alpha\,/\,H^3) + (16\,\beta\,/\,H^2) + (24\,\gamma\,/\,H) + 32\,\delta]\,(h_0\,/\,H)$$

$$= h_0\,[\alpha + 2\,\beta\,H + 3\,\gamma\,H^2 + 4\,\delta\,H^3] = h_0\,(d\,V/d\,H)\ldots\ldots\ldots\ldots\ldots(6.3)$$

Expression for d V/d H (from equation (6.2)) is used in equation (6.3)

ME coefficient is expressed as dE/dH = (1/d) (dV/dH)

Using equation (6.3) the **ME coefficient** (dE/dH) can be express as

$$\textbf{dE/dH = (1/t) (V}_{\textbf{out}} \textbf{ / h}_0\textbf{)}\dots\dots\dots\dots\dots\text{(6.4)}$$

Where t is the effective thickness of the sample [Giap et al. (2007)]

6.5. Results and Discussion

6.5.1. Room Temperature Crystal Structure of Composites

Fig.6.2 depicts the XRD profile of $(1-y)0.51Bi(Ni_{1/2}Ti_{1/2})O_3-$ $0.49PbTiO_3/yNi_{0.6}Zn_{0.4}Fe_2O_4$ (BNT-PT/NZFO) composites for the composition range y=0 to 1.0 at an composition interval of 0.1. The XRD peaks corresponding to the ferroelectric phase BNT-PT and spinel cubic NZFO phase are marked by 'b' and 'n', respectively. As can be seen in Fig.6.2, no impurity phases have formed during composite formation and all the peaks are due to ferrite and ferroelectric phases. As the fraction of NZFO phase is increased, the intensity of XRD profiles corresponding to cubic spinel NZFO increases while the intensity of the XRD profiles corresponding to tetragonal perovskite BNT-PT decreases. All the XRD peaks corresponding to tetragonal perovskite phase of BNT-PT and spinel cubic phase of NZFO are indexed in the Fig.6.2 which suggests the formation of ideal composite. No signature of any impurity phase is observed in the powder XRD pattern. Two phase structure refinement corresponding to ferrite and ferroelectric phases indicates that no additional phase is formed during the composite formation.
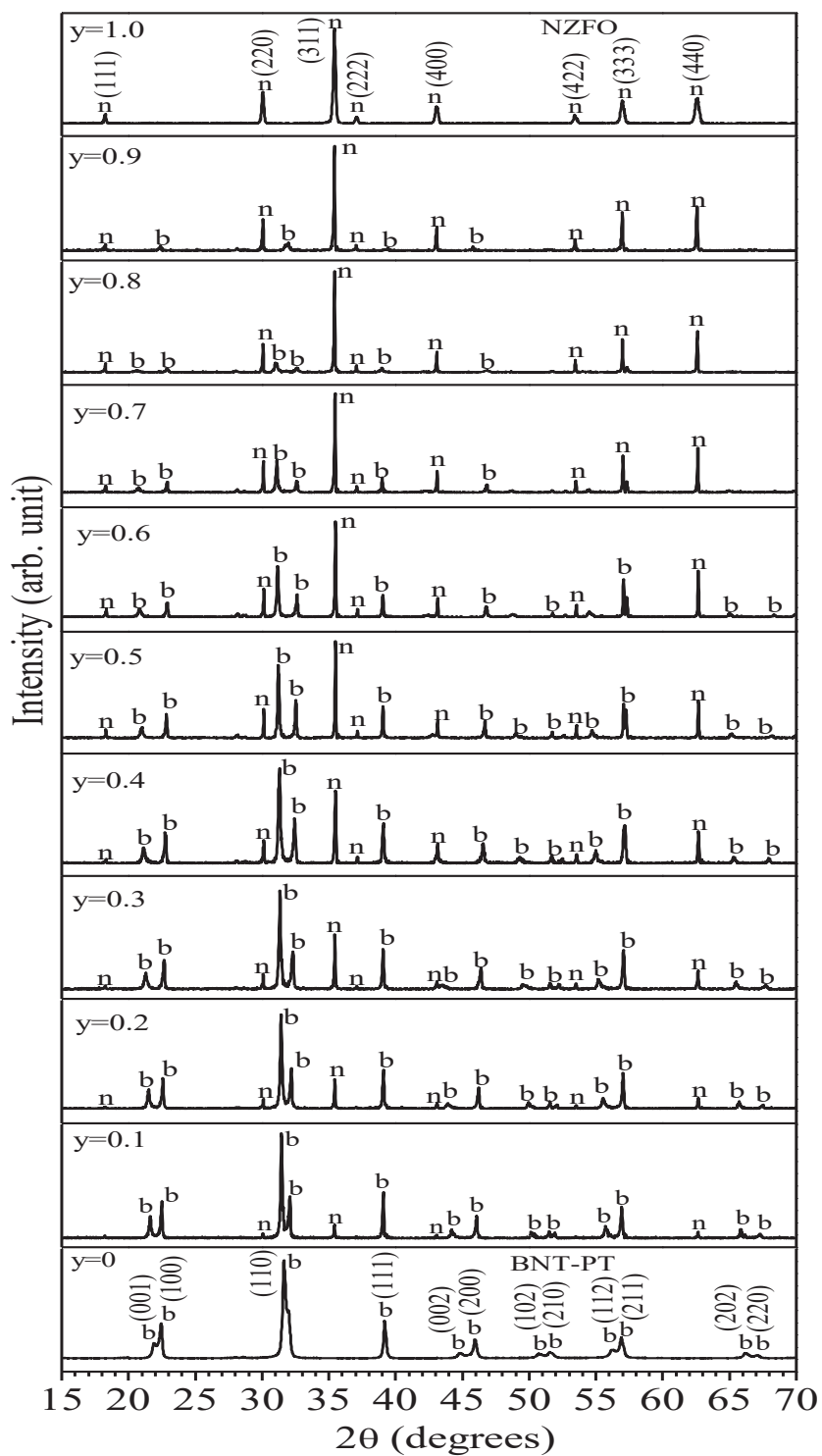
Fig.6.2. Powder XRD patterns of (1-y)BNT-PT/yNZFO particulate composites for the composition with y=0, 0.1, 0.2, 0.3, 0.4, 0.5, 0.6, 0.7, 0.8, 0.9 and 1.0 sintered at 1000^{0}C for 3 hours. Peaks corresponding to BNT-PT are marked by 'b' and NZFO by 'n'.

We carried out Rietveld structure refinement for all the compositions of composite to check the phase purity and determine structural parameters precisely. Fig.6.3 shows the Rietveld fit for the composition with y=0.5. Very good fit between the observed and calculated XRD profiles confirms the presence of ferroelectric tetragonal and ferrite cubic structure without any impurity. Refined structural parameters for the composition with y=0.5 are listed in Table 6.1.

To study the effect of composite formation on the structure of BNT-PT, we show in Fig.6.4 the (200)/(002) XRD profiles of the BNT-PT phase in the composite for the compositions with y=0, 0.2, 0.4, 0.6, 0.8 and 0.9. It is evident from this figure that the tetragonality of BNT-PT significantly increases when the fraction of NZFO is increased in the composite. The tetragonality of pure BNT-PT is 1.02 [Pandey and Singh (2014)] which is significantly lower than the tetragonality 1.06 of $PbTiO_3$ [Jaffe et al. (1971)]. The tetragonality increases upto 1.11 (~ 9%) for the composite in the composition y=0.8. The unusual increase in the tetragonality of BNT-PT may occur due to the diffusion of Fe^{3+} or Zn^{2+} ions at the B-site of the ferroelectric phase BNT-PT in the composites. On further increasing the fraction of NZFO (for the composition y=0.9), the structure of BNT-PT changes in to rhombohedral ($R\bar{3}c$) phase (as shown in Fig.6.5). Clear splitting in the (111) pseudocubic reflection suggests that the structure is rhombohedral which is singlet in the case of tetragonal phase.

Table.6.1. Refined structural parameters obtained by Rietveld analysis of BNT-PT/NZFO composite with y=0.5 using tetragonal P4mm and cubic Fd$\overline{3}$m space groups.

Space Group	Ions	Positional coordinates			Thermal parameters B(Å^2)
		x	y	z	
Fd$\overline{3}$m	Zn^{+2} / Fe$_I^{+3}$	0.125	0.125	0.125	1.0 (1)
	Fe$_{II}^{+3}$/ Ni^{+2}	0.5	0.5	0.5	1.2 (1)
	O^{-2}	0.2585(6)	0.2585(6)	0.2585(6)	1.2 (2)
			a=8.3564(2)Å		
P4mm	Bi^{3+}/Pb^{+2}	0.0	0.0	0.0	3.1(1)
	Ni^{2+}/Ti^{+4}	0.5	0.5	0.545(4)	0.7(2)
	O$_I^{-2}$	0.5	0.5	0.162(2)	1.2(1)
	O$_{II}^{-2}$	0.5	0.0	0.646(4)	0.8(1)
			a=b=3.888(2)Å, c=4.223(3)Å		
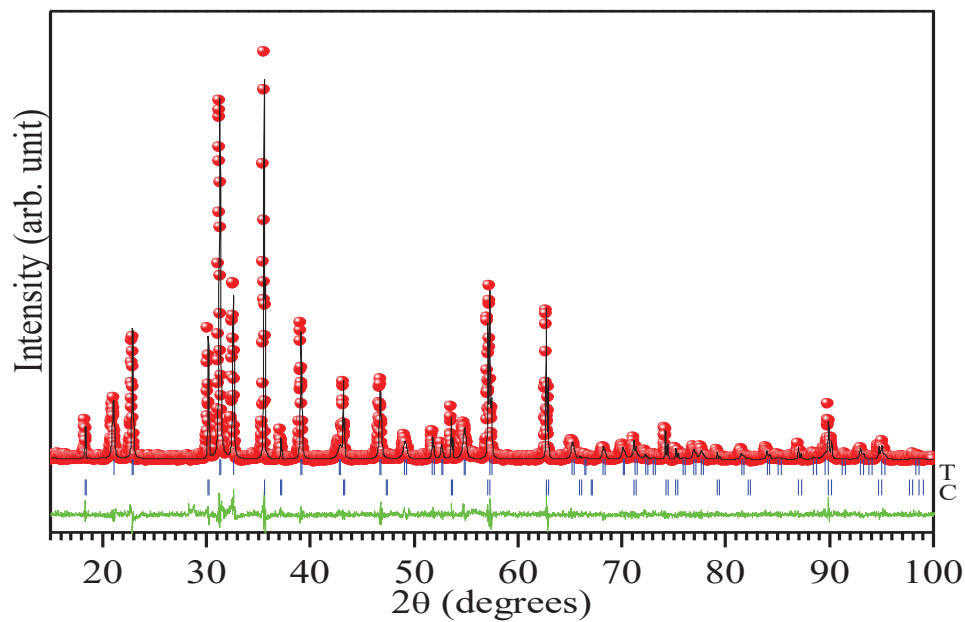
Fig.6.3. Experimentally observed (dots), Rietveld calculated (continuous line), and difference (bottom line) profiles obtained after the Rietveld refinement of the structure of particulate composite for the composition with y=0.5 sintered at 1000^{0}C using coexisting [Cubic (Fd$\bar{3}$m) + Tetragonal (P4mm)] phases. The vertical tick-marks above the difference plot show the positions of the Bragg-peaks.
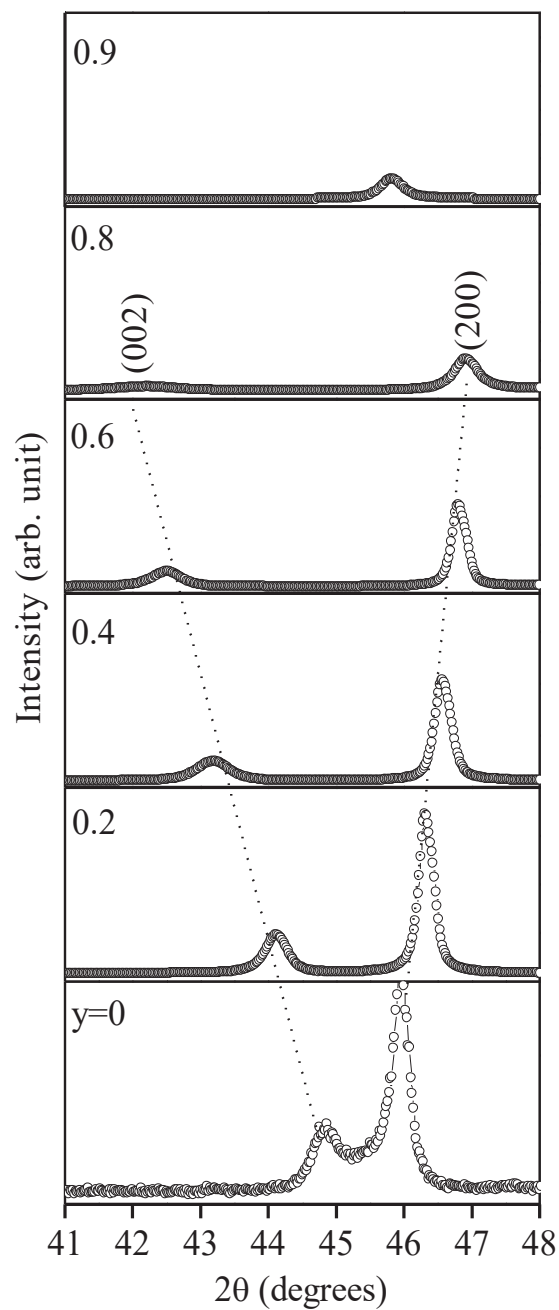
Fig.6.4. (002)/(200) XRD profiles of ferroelectric phase (BNT-PT) extracted from XRD data of $(1-y)0.51Bi(Ni_{1/2}Ti_{1/2})O_3-0.49PbTiO_3/yNi_{0.6}Zn_{0.4}Fe_2O_4$ composite using Rietveld fitting for the compositions y=0, 0.2, 0.4, 0.6, 0.8 and 0.9.

Enhancement in the tetragonality of $(1-x)Bi(Zn_{1/2}Ti_{1/2})O_3$-$xPbTiO_3$ is observed with increasing $Bi(Zn_{1/2}Ti_{1/2})O_3$ concentration [Suchomel and Davies (2005)]. Similarly, enhancement in the tetragonality of $(1-x)BiFeO_3$-$xPbTiO_3$ is observed with the increasing $BiFeO_3$ concentration [Bhattacharjee and Pandey (2010)] which finally turns in to rhombohedral ($R\bar{3}c$) phase for high concentration of $BiFeO_3$ [Bhattacharjee et al. (2007)]. On the basis of XRD patterns shown in Fig.6.4 and reported results by earlier authors [Suchomel and Davies (2005); Bhattacharjee and Pandey (2010); Bhattacharjee et al. (2007)] it can be concluded that diffusion of Fe^{3+}/Zn^{2+}ions is taking place from NZFO to ferroelectric BNT-PT phase. To confirm the structure for the composition with y=0.9, we carried out Rietveld structure refinement using $R\bar{3}c$ space group for the ferroelectric phase (BNT-PT). As shown in Fig. 6.5. good fit between observed and calculated profiles confirms the rhombohedral structure for the ferroelectric phase of the composite composition with y=0.9.

The variation of lattice parameters and tetragonality of ferroelectric phase BNT-PT with composite composition in the composition range y=0 to 0.8 are shown in Fig6.6(a). The 'c' lattice parameter of the ferroelectric phase BNT-PT increases while 'a' lattice parameter decreases with increasing NZFO concentration upto y=0.8 in the (1-y)BNT-PT/yNZFO composites. The lattice parameter of NZFO also increases with increasing the NZFO content in the composite as shown in Fig.6.6(b). This suggests that the diffusion of ions from ferroelectric phase BNT-PT to magnetic phase NZFO is taking place to modify the lattice parameter after the composite formation.
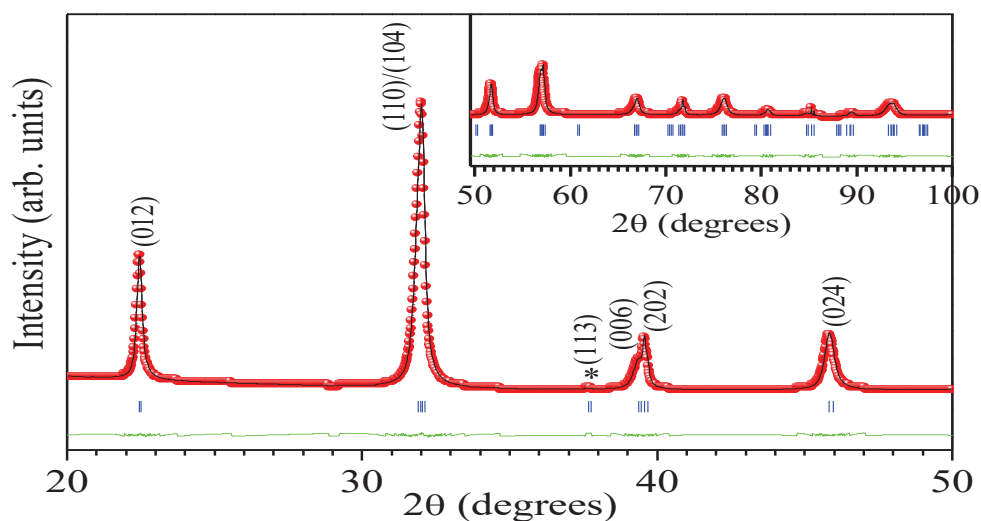
Fig.6.5. Experimentally observed (dots), calculated (continuous line), and difference (bottom line) profiles obtained after the Rietveld refinement of ferroelectric phase BNT-PT of BNT-PT/NZFO composite for the composition with y=0.9 using rhombohedral (R$\bar{3}$c) structure. Asterisk shows the superlattice reflection (113). The vertical tick-marks above the difference plot show the positions of the Bragg-peaks.
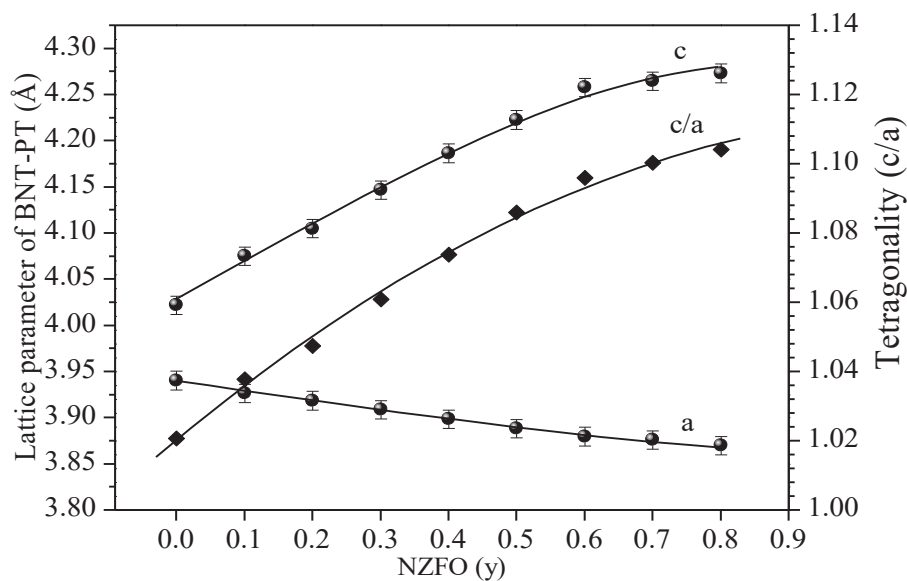

Fig.6.6. (a) Variations of lattice parameters (a, c) and tetragonality (c/a) of ferroelectric phase BNT-PT in (1-y)BNT-PT/yNZFO composites for the compositions with y=0 to 0.8.

161
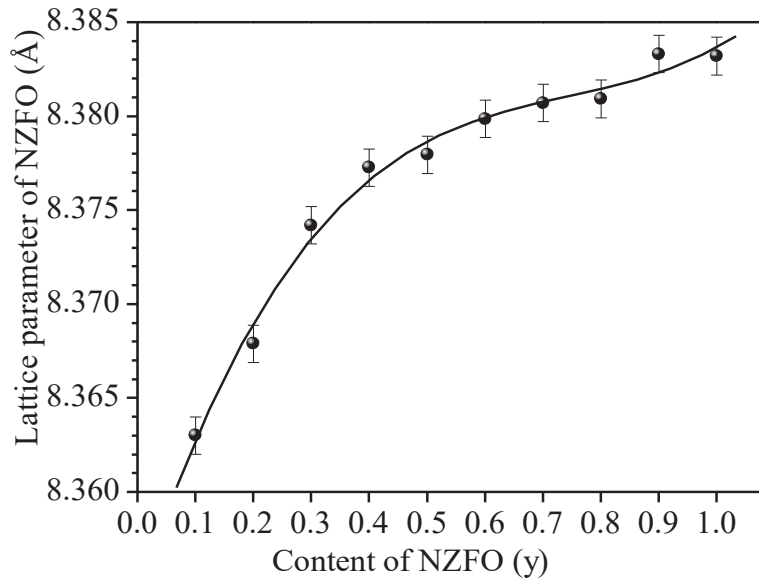
Fig.6.6. (b) Variation of lattice parameter with composites compositions for the magnetic spinel phase NZFO in (1-y)BNT-PT/yNZFO.
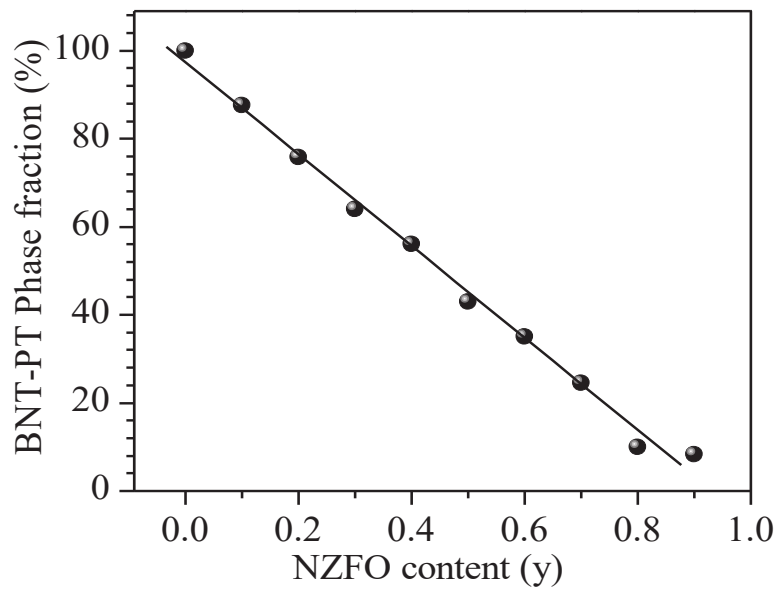
Fig.6.6. (c) Variation of phase fraction (%) of ferroelectric BNT-PT with composition in (1-y)BNT-PT/yNZFO composites.

It has been reported [Globus et al. (1977); Valenzuela (2005)] that the lattice parameter of NZFO increases with increasing the Zn concentration. The variation of phase fraction of BNT-PT calculated from Rietveld refinement for the (1-y)BNT-PT/yNZFO composites is shown in Fig.6.6(c). As expected, linear decrease in the phase fraction of ferroelectric phase BNT-PT is observed with increasing the fraction of NZFO in the composites. Obviously the phase fraction of NZFO should increase with increasing the fraction of NZFO in (1-y)BNT-PT/yNZFO composites. Phase fractions were found in good agreement with weight fractions used for synthesis, suggesting the formation of ideal composites.

6.5.2. SEM and EDS Studies

SEM and EDS spectrum for the composite compositions with y=0.3 and 0.7 are shown in Figs.6.7.(a-f). Two types of particle morphology corresponding to magnetic NZFO and ferroelectric BNT-PT can be clearly distinguished from the SEM image. Particles with dark and white appearance correspond to magnetic NZFO and ferroelectric BNT-PT phases, respectively. EDS spectrum of the white grains for composition with y=0.3 (Fig.6.7(c)) reveals the presence of Ni, Zn, Fe ions correspond to ferrite phase. EDS spectrum of the dark grains for composition with y=0.3 (Fig.6.7(d)) reveals the presence of Bi, Ni, Ti, and Pb ions from the ferroelectric phase. Similarly, the EDS spectrum of the white grains for the composition with y=0.7 (Fig.6.7(e)) reveals the presence of Ni, Zn, Fe ions corresponding to the ferrite phase. EDS Spectrum of the dark grains for the composition with y=0.7 (Fig.6.7(f)) reveals the presence of Bi, Ni, Ti, and Pb ions corresponding to the ferroelectric phase. EDS spectrum of both the

compositions with y=0.3 and 0.7 depicts the presence of Ti ions in magnetic NZFO phase and Fe ions in ferroelectric BNT-PT phase. The above phenomenon reveals the ionic diffusion between ferroelectric and magnetic phase in BNT-PT/NZFO composite.
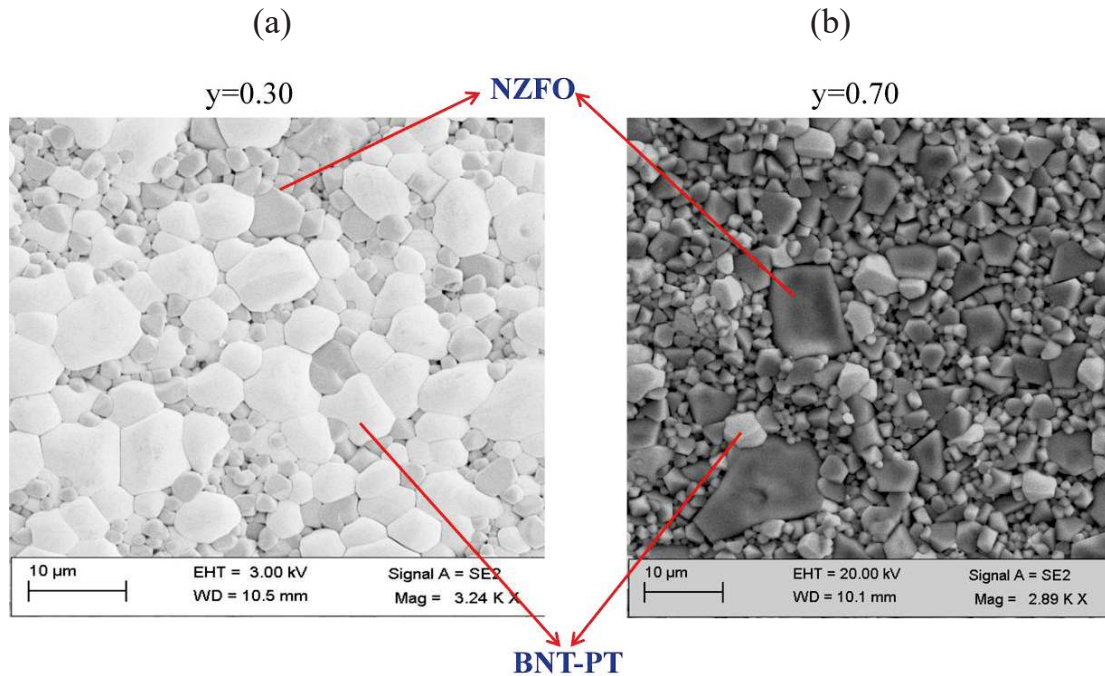

Fig.6.7. SEM image for $(1-y)0.51Bi(Ni_{1/2}Ti_{1/2})O_3-0.49PbTiO_3/yNi_{0.6}Zn_{0.4}Fe_2O_4$ composite with (a) y=0.3 and (b) y=0.7 where grains with dark appearance correspond to $Ni_{0.6}Zn_{0.4}Fe_2O_4$ (NZFO) and white appearance correspond to ferroelectric $0.51Bi(Ni_{1/2}Ti_{1/2})O_3-0.49PbTiO_3$ (BNT-PT) phases.
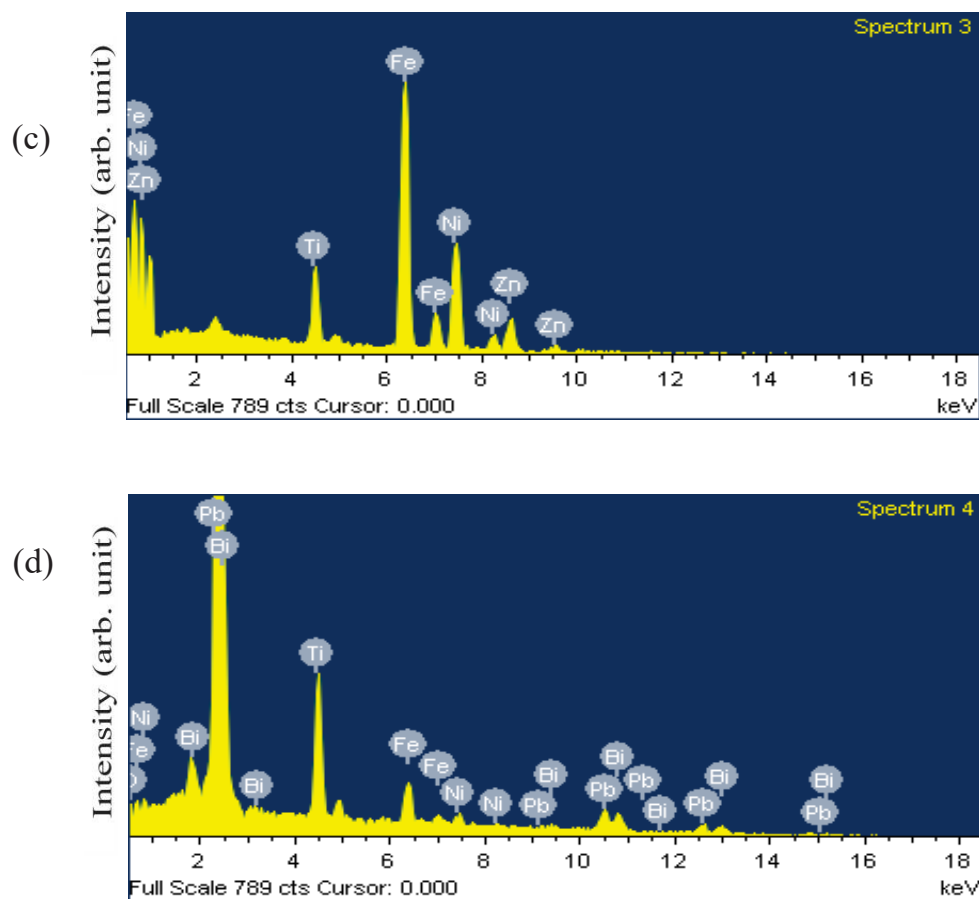
Fig.6.7. EDS spectrum for (c) ferrite NZFO and (d) ferroelectric BNT-PT phases for the $(1-y)0.51Bi(Ni_{1/2}Ti_{1/2})O_3-0.49PbTiO_3/yNi_{0.6}Zn_{0.4}Fe_2O_4$ composite with composition y=0.3. Diffusion of Ti^{4+} ions in NZFO phase from BNT-PT and Fe^{3+} ions in BNT-PT from NZFO is evident from the EDS spectrum.
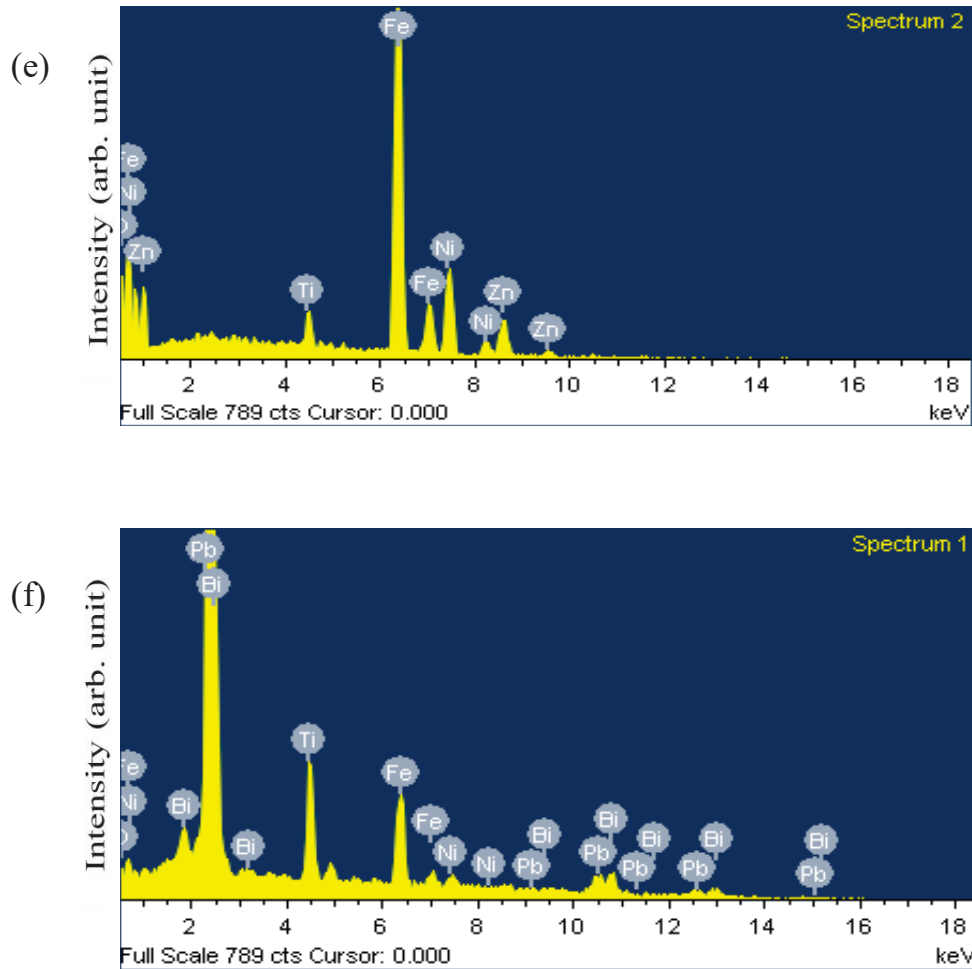
Fig.6.7. EDS spectrum for (c) ferrite NZFO and (d) ferroelectric BNT-PT phases for the $(1-y)0.51Bi(Ni_{1/2}Ti_{1/2})O_3$-$0.49PbTiO_3/yNi_{0.6}Zn_{0.4}Fe_2O_4$ composite with composition y=0.7. Diffusion of Ti^{4+} ions in NZFO phase from BNT-PT and Fe^{3+} ions in BNT-PT from NZFO is evident from the EDS spectrum.

6.5.3. Variation of Grain Size in the Composite

Grain sizes of the ferroelectric and magnetic components of the composites are not constant and changes during composite formation for the different compositions of (1-y)BNT-PT/yNZFO composites. The average grain size of ferroelectric and magnetic phases for composite compositions with y=0.3, 0.7 and 0.8 are listed in Table 6.2. The grain size of the ferroelectric phase is continuously decreasing with increasing NZFO concentration in the composite. In contrasts, the grain size of the ferrite phase NZFO is continuously increasing with increasing its concentration. This suggests that the mechanism of grain growth is significantly getting modified with the composite concentration.

Table.6.2. Average grain size (μm) of ferroelectric (BNT-PT) and magnetic (NZFO) phases for the composite compositions with y=0.3, 0.7 and 0.8.

Composition	Grain size of BNT-PT	Grain size of NZFO
y=0.3	4.93μm	2.14μm
y=0.7	2.69μm	4.86μm
y=0.8	1.57μm	6.37μm

6.5.4. Polarization Studies

Fig.6.8 shows the P-E hysteresis loops for the different compositions of (1-y)BNT-PT/yNZFO composites with y=0, 0.1, 0.3, 0.5, 0.7 and 0.9. All the compositions show ferroelectric hysteresis loop. As expected, the saturation/remanent polarization is decreasing with increasing the NZFO concentration in the composite. The decrease in the saturation/remanent polarization is due to the reduced phase fraction of ferroelectric phase in the composite. The distribution of NZFO in BNT-PT matrix lowers the coercivity since the two phases are uniformly distributed in the composite. Fig.6.9 shows the composition dependence of remnant polarization (P_r). Both the remanat polarization and coercive field are decreasing after the composite formation. The saturation polarization in (1-y)BNT-PT/yNZFO particulate composites investigated in the present work is higher than $xNiFe_2O_4$/(1-x)$Pb_{0.988}(Zr_{0.52}Ti_{0.48})_{0.976}Nb_{0.024}O_3$ composite [Ciomaga et al. (2013)].
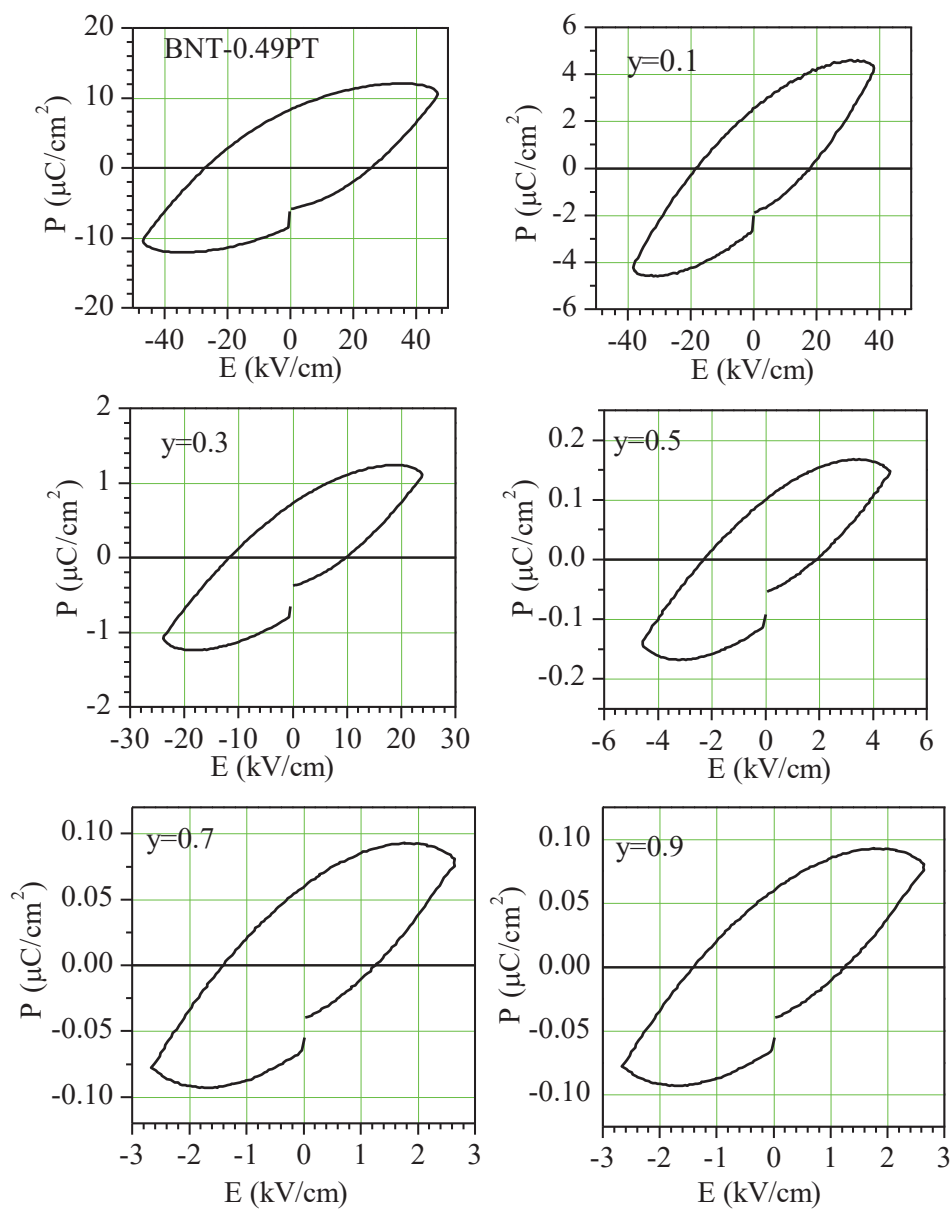
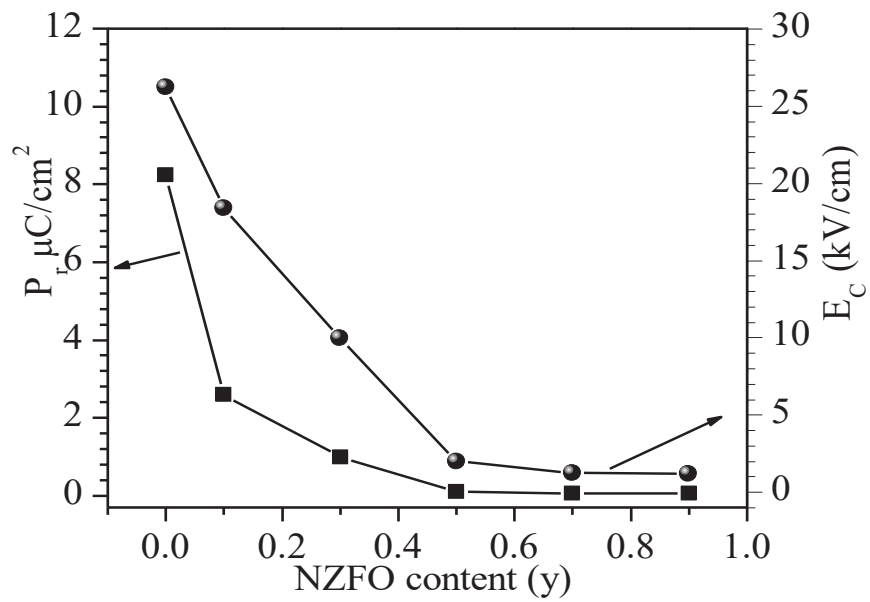**Fig.6.8.** P-E hysteresis loop for (1-y)BNT-PT/yNZFO composites for the compositions with y=0, 0.1, 0.3, 0.5, 0.7 and 0.9.

Fig.6.9. Composition dependence of remanent polarization (P_r) and coercive field (E_C) for (1-y)BNT-PT/yNZFO composites with y=0, 0.3, 0.5, 0.7 and 0.9.

6.5.5. Dielectric Studies

The frequency dependence of dielectric constant at room temperature for for two compositions of (1-y)BNT-PT/yNZFO composites with y=0.2 and 0.9 are shown in Figs.6.10(a,b). The dielectric constant decreases rapidly with increasing frequency in low frequency region and becomes nearly constant in high frequency region. The frequency dependent dielectric dispersion in ferrites based composite is observed due to a space-charge effect which can be explained on the basis of Koop's theory. This may lead to the Maxwell-Wagner type interfacial polarization [Koops (1951)]. The room temperature permittivity ($\varepsilon^{/}$) of the (1-y)BNT-PT/yNZFO composite at 10kHz frequency for different compositions is shown in Fig. 6.10(c). It is evident from Fig. 6.10(c) that permittivity decreases with increasing the concentration of NZFO. Obviously, this is due to the decrease in the fraction of the ferroelectric phase BNT-PT. Another reason for decrease in the dielectric constant with increasing ferrite content may be attributed to the Verwey-type electron exchange polarization [Upadhyay et al. (1996)].
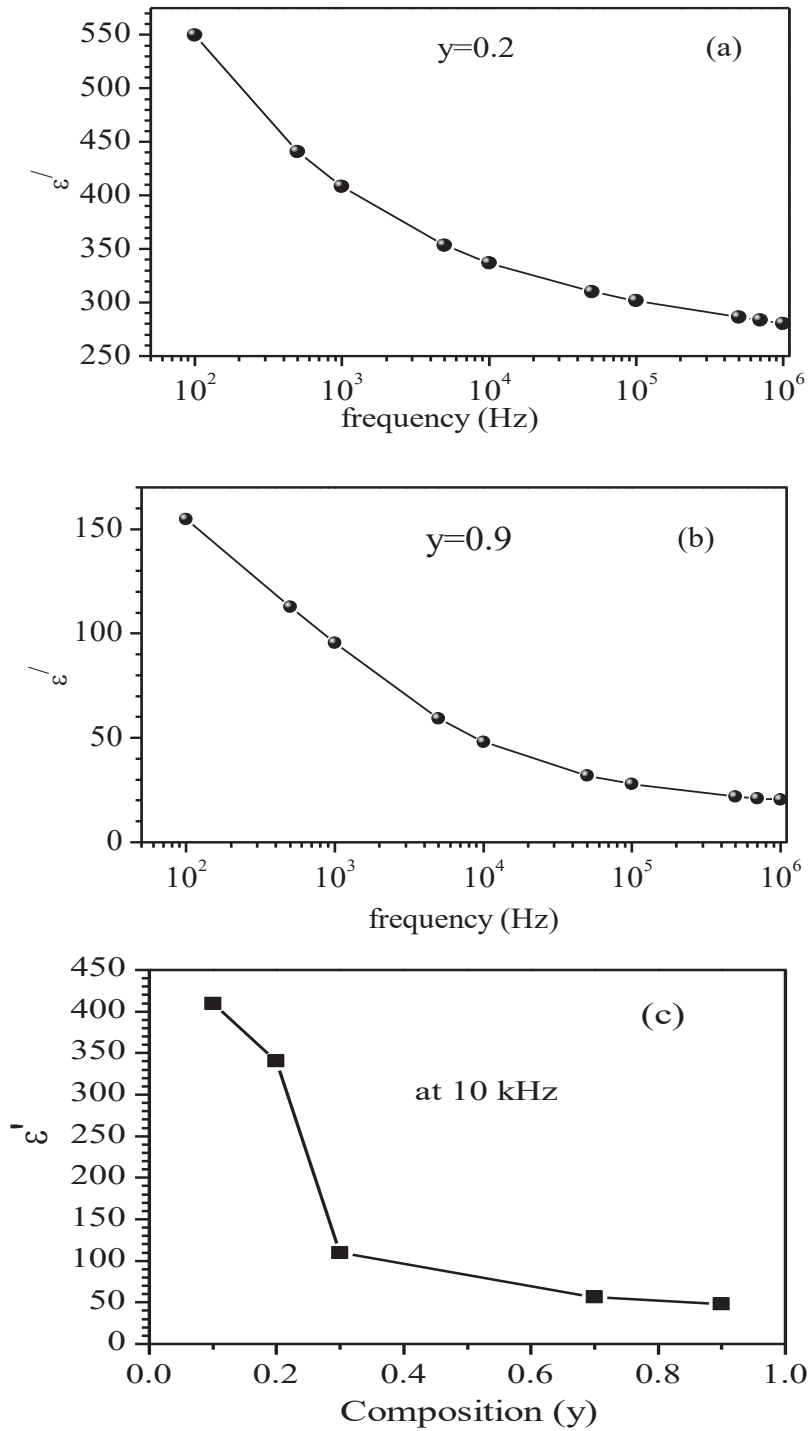
Fig.6.10. Frequency dependent room temperature permittivity ($\varepsilon^{/}$) of (1-y)BNT-PT/yNZFO composites for the compositions with (a) y=0.2 and (b) y=0.9. (c) Composition dependence of room temperature permittivity ($\varepsilon^{/}$) at 10kHz for (1-y)BNT-PT/yNZFO composites.

6.5.6. Magnetic Properties

The room temperature magnetic hysteresis (M-H) loop for (1-y)BNT-PT/yNZFO composites with y=0.4 and 0.8 are shown in Fig.6.11(a) and (b). The hysteresis loops suggest ferrimagnetic behaviour of the sample (inset Figs.6.11(a,b). The saturation magnetization is increasing with increasing the ferrite content in the composite. In the ferrite/ferroelectric particulate composites, when the ferroelectric phase is increased, the contact between ferroelectric and magnetic grains is increased which breaks the magnetic circuit between magnetic phases and thus lowers the magnetization [Adhlakha and Yadav (2012); Kambalea et al. (2010)]. The M-H curves get horizontal at higher applied field for both the compositions with y=0.4 and 0.8.

6.5.7. ME-response of BNT-PT/NZFO Composites

The ME response of (1-y)BNT-PT/yNZFO composites for the compostions with y=0.2, 0.3, 0.5, 0.8 and 0.9 are shown in Fig.6.12(a-e). It is evident from these figures that the ME coefficient (dE/dH) decreases with increasing DC magnetic field. Magnetostriction in the magnetic phase gets saturated at the higher value of applied magnetic field which produces a constant electric field in piezoelectric phase [Praveena and Varma (2014); Jadhav et al. (2010)]. The maximum value of ME-coefficient is found ~ 33mV/cm-Oe for the ferroelectric rich composite composition with y=0.3. ME-coefficient decreases for the magnetic rich compositions with (y=0.8 and 0.9) probably due to lower resistivity of the samples. Similar variations in ME coefficient are reported in $BaTO_3$-$CoFe_2O_4$ [Suryanarayana (1994)], $Ni_{0.5}Co_{0.5}Fe_2O_4$/$Ba_{0.8}Pb_{0.2}TiO_3$ [Kadam

et al. (2005)], $Ba_{0.8}Pb_{0.2}TiO_3$- $Cu_{0.4}Co_{0.6}Fe_2O_4$ [Kothale et al. (2005)], $Ni_{0.3}Cu_{0.4}Zn_{0.3}Fe_2O_4$/ $BaTiO_3$-PZT [Jadhav et al. (2010)], $Ni_{0.9}Zn_{0.1}Fe_2O_4$/PZT [Chougule et al. (2008)] multiferroic particulate composites.
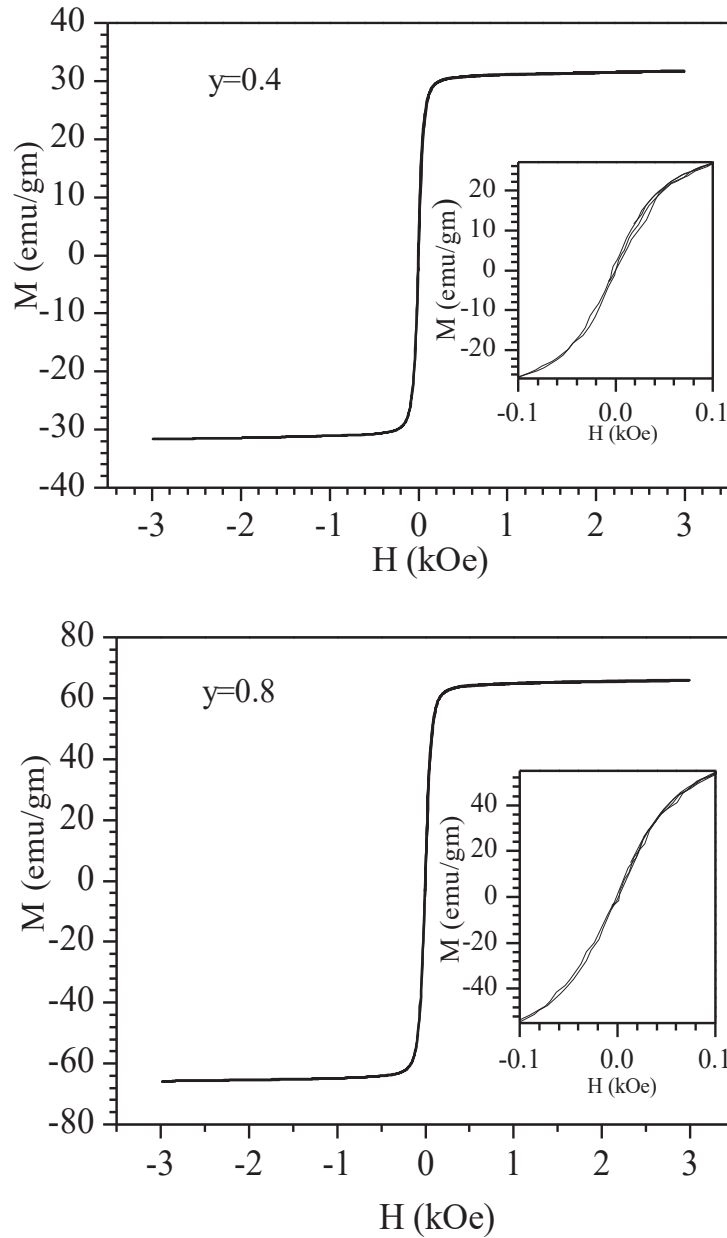

Fig.6.11. Room temperature magnetic hysteresis loops of BNT-PT/NZFO (y=0.4 and 0.8). Insets show the magnified view of the M-H hysteresis loops.
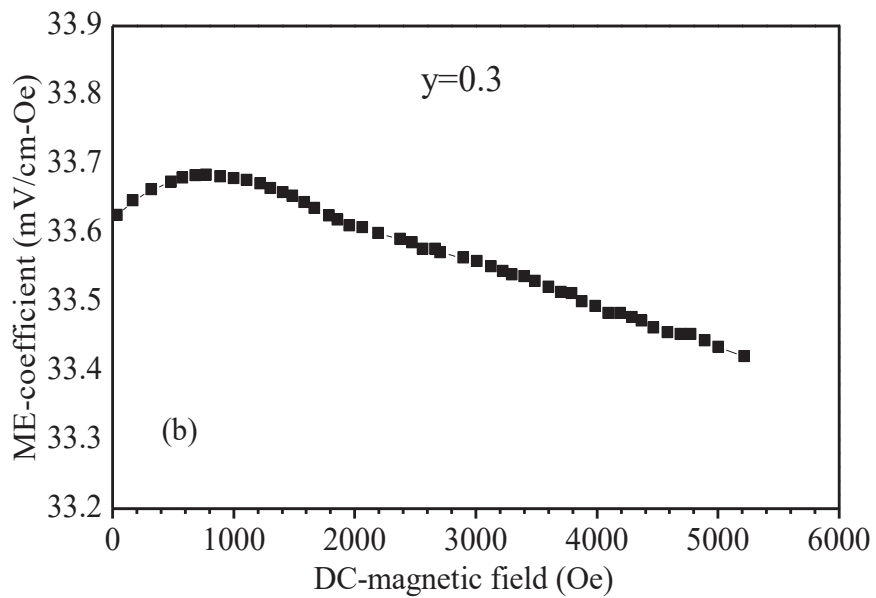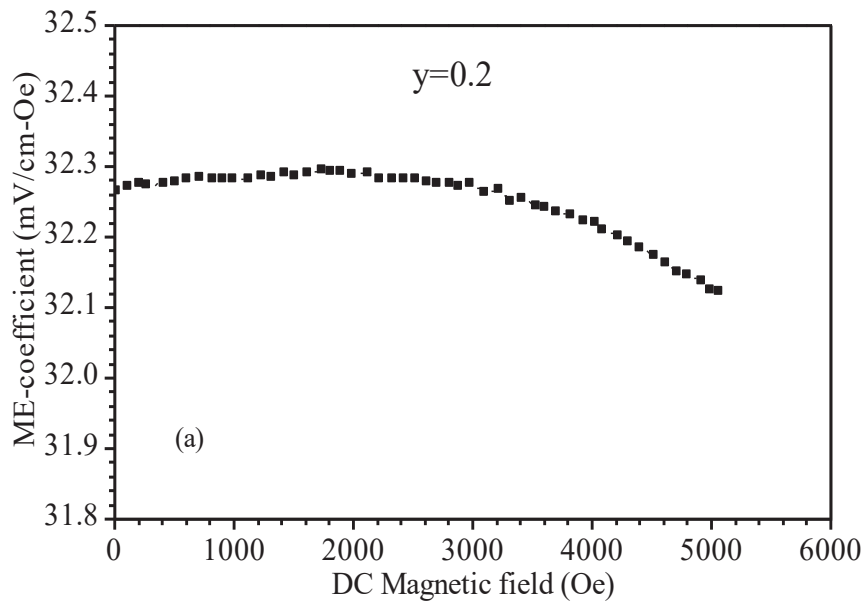
Fig.6.12. ME-coefficient (mV/cm-Oe) of (1-y)BNT-PT/yNZFO composite for the composition with (a) y=0.2 and (b) y=0.3.
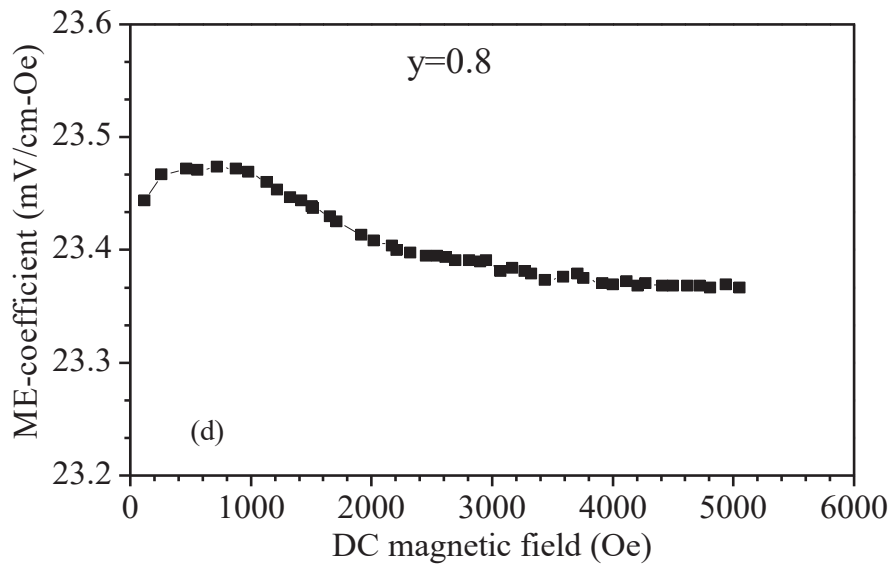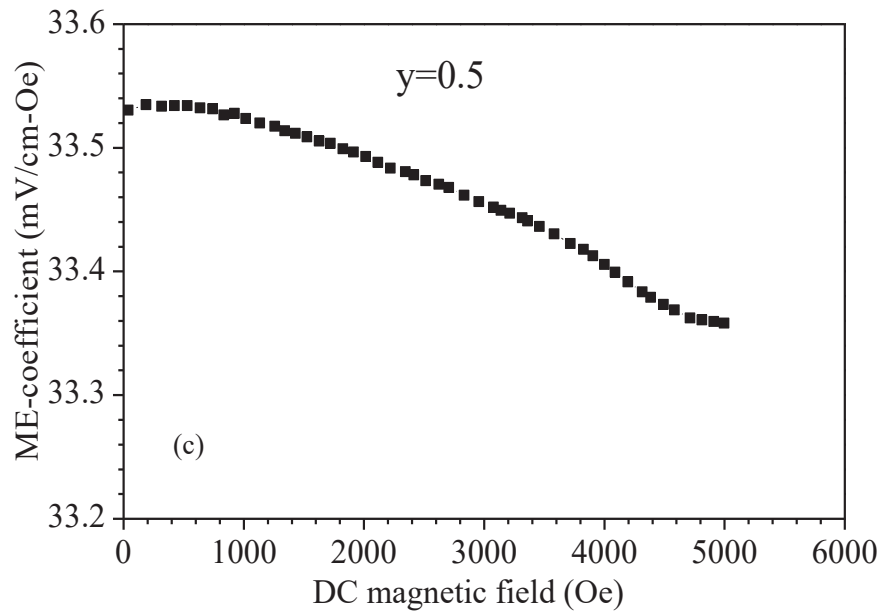
Fig.6.12. ME-coefficient (mV/cm-Oe) of (1-y)BNT-PT/yNZFO composites for the composition with (c) y=0.5 and (d) 0.8.
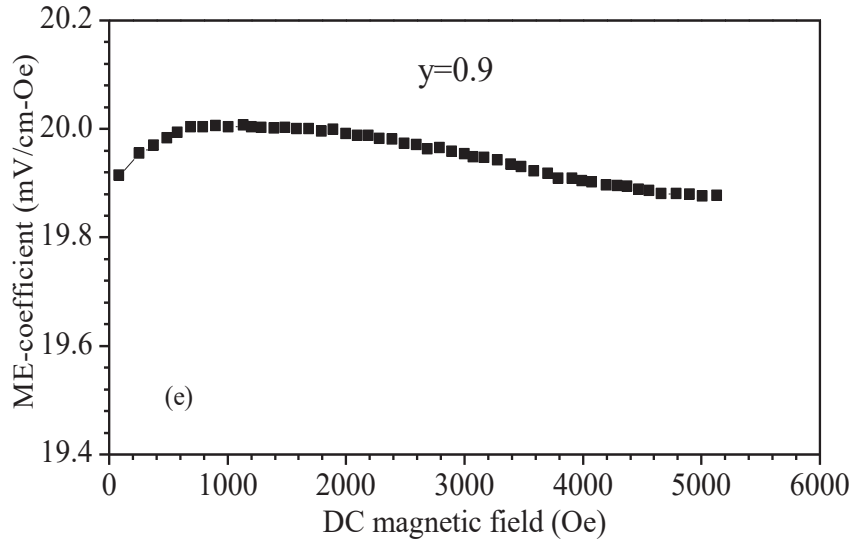
Fig.6.12(e). ME-coefficient (mV/cm-Oe) of (1-y)BNT-PT/yNZFO composite for the composition with y=0.9.

6.6. Discussion

Although the clear theoretical explanation of ME behavior in particulate composites is unknown, several theoretical models such as Green function method, first principle density functional theory and phase field models have been proposed to understand the ME response in composites [Nan et al. (2008)]. As discussed in Chapter I, Nan et al. [Nan et al. (2008)] have described the properties of composite materials using Green function and perturbation theory. These authors have shown that theoretical results using Green function and perturbation theory are in good agreement with the cubic model [Nan et al. (2008)]. Phase transformation behaviour in the ferroelectric phase plays an

important role in the enhancement of the ME properties in the composites. Phase transformation that introduces the strain in the ferroelectric phase provides better coupling between the two phases. In the laminate composite of $La_{0.67}Sr_{0.33}MnO_3$ and $BaTiO_3$, the substrate $BaTiO_3$ undergoes a phase transition from the tetragonal phase to monoclinic phase at the temperature 278K. The structural transformation in $BaTiO_3$ substrate develops huge magnetization (70%) where the strain changes only 1% [Eerenstein et al. (2006)]. In BNT-PT/NZFO strain is changing by 9% for the composition with y=0.9 which exhibit significant ME-coefficient. Enhancement in the tetragonality of ferroelectric phase is linked by the diffusion of Fe^{3+} or Zn^{2+} ions at the B-site of the perovskite similar to (1-x)$Bi(Zn_{1/2}Ti_{1/2})O_3$-$xPbTiO_3$ [Suchomel and Davies (2005)] and (1-x)$BiFeO_3$-$xPbTiO_3$ [Bhattacharjee et al. (2007); Bhattacharjee and Pandey (2010)] perovskite solid solutions. The (1-x)$Bi(Zn_{1/2}Ti_{1/2})O_3$-$xPbTiO_3$ and (1-x)$BiFeO_3$-$xPbTiO_3$ solid solutions are the special kind of perovskites in which the tetragonality decreases with increasing the $PbTiO_3$ content and BZT or BF rich compositions exhibit large tetragonality. This phenomenon is completely opposite to the $PbZr_xTi_{1-x}O_3$ [Ragini et al. (2001)], (1-x)$Pb(Mg_{1/3}Nb_{2/3})O_3$-$xPbTiO_3$ [Singh and Pandey (2003)], (1-x)$Pb(Sc_{1/2}Nb_{1/2})O_3$-$xPbTiO_3$ [Haumont et al. (2005)] and (1-x)$Bi(N_{1/2}Ti_{1/2})O_3$-$xPbTiO_3$ [Pandey and Singh (2014)] solid solutions where the tetragonality increases with increasing the PT concentration. Unusually large tetragonality in the BZT has been explained as the large coordination at the B-site cations [Suchomel et al. (2006)]. In BF-PT high tetragonality has been explained by covalent character of 'B-O' bonds which

increases the tetragonality [Bhattacharjee et al. (2007)]. Thus, our results of XRD, EDS and earlier reports [Bhattacharjee et al. (2007); Bhattacharjee and Pandey (2010); Suchomel and Davies (2005)] strongly suggest that the diffusion of Fe^{3+} and Zn^{2+}ions in the ferroelectric phase of BNT-PT/NZFO composite is leading to enhancement in the tetragonality of ferroelectric phase.

6.7. Summary

The structural characterization of (1-x)BNPT/xNZFO composites reveal that no secondary phases appear after composites formation. The lattice parameters of both the ferrite and ferroelectric phases are modified and show composition dependence in the composites suggesting that the ions from the two phases diffuse to each other during sintering. The tetragonality of the ferroelectric phase continuously increases with increasing the ferrite fraction upto 80% in the composites. The SEM characterization reveals well connected separate grains of ferrite and ferroelectric phases in the composite. All the compositions of the composite investigated in the present work exhibit ferroelectric hysteresis loop. The magnetic characterization of the composite reveals ferrimagnetic behaviour. The maximum value of ME-coefficient is found as ~ 33mV/cm-Oe for the ferroelectric rich composite composition with 30% magnetic ferrite phase.